ACS Energy LETTERS

http://pubs.acs.org/journal/aelccp

Nanoporous GaN/*n*-type GaN: A Cathode Structure for ITO-Free Perovskite Solar Cells

Kwang Jae Lee,[+] Jung-Wook Min,[+] Bekir Turedi, Abdullah Y. Alsalloum, Jung-Hong Min, Yeong Jae Kim, Young Jin Yoo, Semi Oh, Namchul Cho, Ram Chandra Subedi, Somak Mitra, Sang Eun Yoon, Jong H. Kim, Kwangwook Park, Tae-Hoon Chung, Sung Hoon Jung, Jong H. Baek, Young Min Song, Iman S. Roqan, Tien Khee Ng, Boon S. Ooi,* and Osman M. Bakr*

Cite This: *ACS Energy Lett.* 2020, 5, 3295−3303

Read Online

ACCESS | Metrics & More | Article Recommendations | Supporting Information

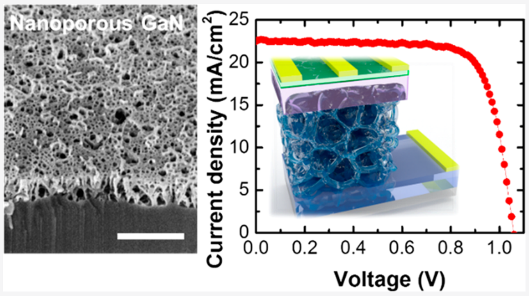

ABSTRACT: Introducing suitable electron/hole transport layers and transparent conductive layers (TCLs) into perovskite solar cells (PSCs) is key to enhancing the selective extraction of charge carriers and reducing surface recombination losses. Here, we introduce nanoporous gallium nitride (NP GaN)/*n*-type GaN (*n*-GaN) as a dual-function cathode structure for PSCs, acting as both the TCL and the electron transport layer (ETL). We demonstrate that the hierarchical NP GaN structure provides an expanded interfacial contact area with the perovskite absorber, while the *n*-GaN under the NP GaN displays high transmittance in the visible spectrum as well as lateral electric conductivity higher than that of a conventional ITO film. Prototype $MAPbI_3$ PSCs based on this NP GaN/*n*-GaN cathode structure (without an extra ETL) show a power conversion efficiency of up to 18.79%. The NP GaN/*n*-GaN platform demonstrated herein paves the way for PSCs to take advantage of the widely available heterostructures of mature III-nitride-based technologies.

Halide perovskites with the general formula AMX_3 (where A = $CH_3NH_3^+$, $CH(NH_2)_2^+$, Cs^+; M = Pb^{2+}, Sn^{2+}; X = I^-, Br^-, Cl^-) have surged to the forefront of optoelectronic materials primarily because of the outstanding performance of perovskite solar cells (PSCs).[1−8] Bandgap tunability (1.5−3.1 eV), a high absorption coefficient ($10^4 - 10^5$ cm^{-1}), low exciton binding energy (<50 meV), and simplicity of fabricationare some of the few properties that played a key role in cementing the place of halide perovskites among solar cell materials.[9−14] However, because dopant−host interactions in perovskites are distinct from those of traditional semiconductor materials (for example, Si:B, GaAs:Mg, and AlN:Si),[15−17] perovskites have not yet been formed into *p-i-n* junctions through doping. Thus, heterogeneous materials need to be integrated to create junctions that promote the charge extraction and collection in PSCs. In this respect, one of the critical issues concerning the fabrication of PSCs is designing the most suitable cathode structure by combining key material components for the extraction of photogenerated electrons, such as an electron transport layer (ETL) and a transparent conductive layer (TCL, cathode electrode).

In PSC cathodes, the ETL is specially designed not only to extract photocurrent but also to exhibit chemical and physical properties commensurate with those of the rest of the PSC structure, such as chemical durability, interfacial properties, thermal/electrical conductivities, bandgap alignment, and optical properties (e.g., refractive index and transmittance).[18−20] TiO_2,[19] ZnO,[20] SnO_2,[21] and $SrSnO_3$[22] are the best-known starting materials for forming ETLs; however, these wide-bandgap oxide materials have several disadvantages, which may include poor electron mobility,[19−22] chemical instability in acid/base solutions,[23] reactivity with the perovskite layer,[23] and high-temperature processing,[24,25] as well as difficulty in tuning band structure, particle size, and film morphology.[26]

Besides the ETL, a TCL such as indium tin oxide (ITO) is an essential part of a PSC for extracting photogenerated charge carriers from the perovskite solar absorber.[2,27,28] The two requirements for a suitable TCL are high transmittance, to deliver more light to the perovskite absorber, and high electrical conductivity, to extract photogenerated electrons more efficiently through the horizontal current path.[28]

Received: July 28, 2020
Accepted: September 17, 2020
Published: September 17, 2020

https://dx.doi.org/10.1021/acsenergylett.0c01621
ACS Energy Lett. 2020, 5, 3295−3303

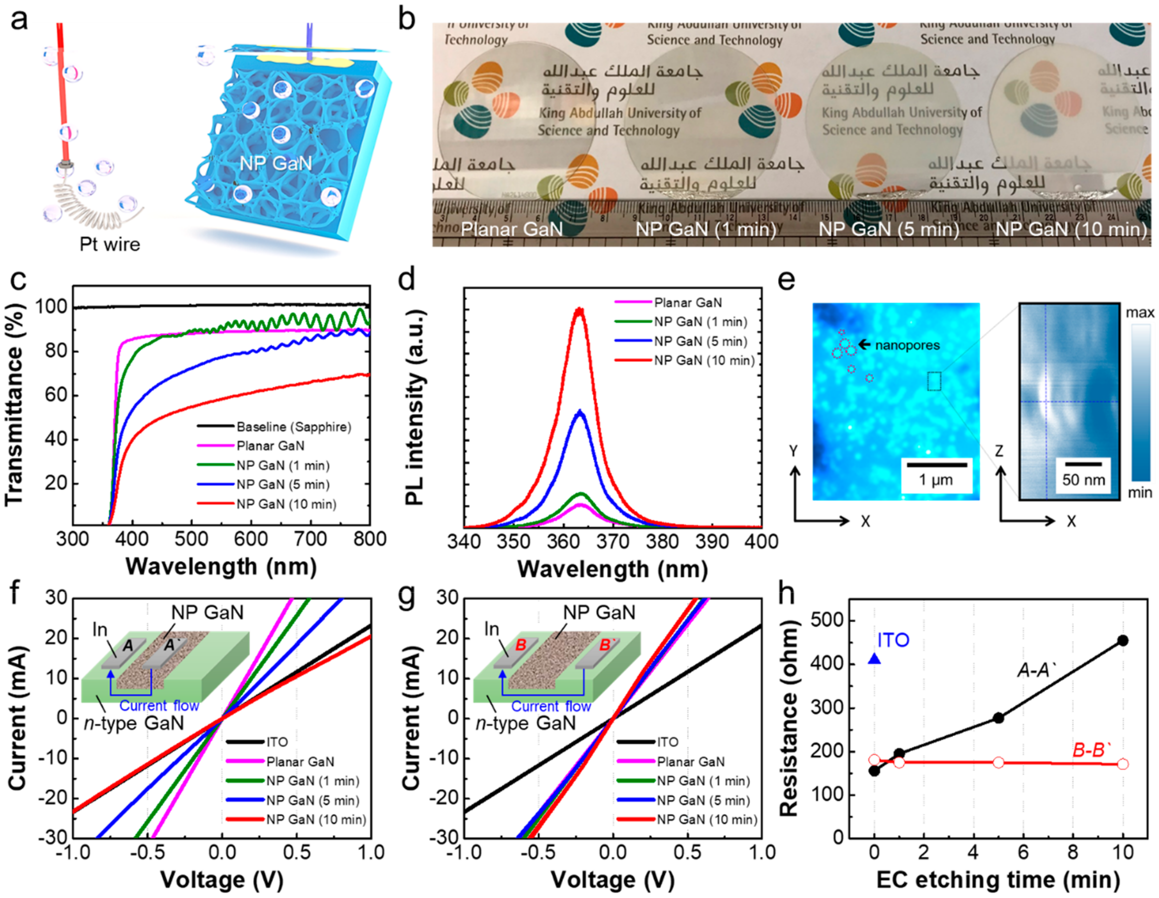

Figure 1. (a) Schematic diagram of electrochemical etching process for NP GaN. (b) Photographs of NP GaN obtained at various electrochemical etching times. (c) Transmittance of NP GaN as a function of electrochemical etching time. (d) PL spectra of NP GaN as a function of electrochemical etching time. (e) Confocal PL images of photons generated by nanopore-induced Rayleigh scattering. Current–voltage curve (f) through the NP GaN region; here the current flow through NP GaN is denoted as A–A′, (g) lateral electrical transport under the NP GaN layer (denoted as B–B′), and (h) resistances of NP GaN as a function of electrochemical etching time.

Unfortunately, during the past decade, the price of ITO has continuously risen because of the scarcity of indium, which may be depleted within the next decade.[29−31]

Gallium nitride (GaN) possesses excellent optical and electrical properties because of its direct bandgap ($E_g \approx 3.4$ eV), transmittance exceeding 82% over the entire visible wavelengths, and high electron mobility (~1000 $cm^2/(V\ s)$).[32] Facile control over the doping type at the desired carrier concentrations and the ease of E_g tuning with alloys ($Ga_xAl_yIn_{1-x-y}N$) allow for versatile tailoring of GaN's electrical and optical characteristics.[33] Furthermore, the thermal, mechanical, and chemical stability of GaN enable practical applications of light-emitting diodes (LEDs),[34,35] laser diodes (LDs),[36] and photodetectors (PDs).[37] These desired characteristics have attracted researchers to study the combination of GaN with perovskites for new concepts of device applications such as piezo-phototronics, photovoltaics, and nanostructured LDs.[38−42]

GaN is generally grown by metal–organic chemical vapor deposition (MOCVD),[43] hydride vapor phase epitaxy (HVPE),[44] molecular beam epitaxy (MBE),[45] or one of other analogous pathways.[46,47] The latest growth technologies have demonstrated their capacity for mass producing GaN wafers (>12 in.) with high throughput, low fabrication costs, and the ability to grow films not only on monocrystalline substrates but also on noncrystalline substrates such as glass and flexible polymer substrates.[48−50] Compared to existing commercialized cathode structures, the price of GaN/substrate is competitive and is likely to decrease with further adoption (Table S1). While some studies have demonstrated potential advantages of GaN for perovskite technology, such as improved stability[38] or the use of GaN as an ETL material[39−41] in current device architectures, it is by eliminating undesirable heterogeneous interfaces, simplifying the device fabrication process, and expanding the design versatility of perovskite devices that GaN, arguably, could have the largest impact (by taking advantage of its versatile doping in combination with its monolithic growth processes).

Motivated by this goal, we introduce nanoporous (NP) GaN epitaxially grown on *n*-type GaN (*n*-GaN), referred to here as (NP GaN/*n*-GaN), as a dual-function cathode structure containing both the TCL and the ETL for spin-coated methylammonium lead iodide ($MAPbI_3$) PSCs. Our finite-difference time-domain (FDTD) and rigorous coupled-wave analysis (RCWA) simulations show that this structure enhances photon harvesting in the cell because of the gradual change in the effective refractive index through the NP GaN/$MAPbI_3$ layer. While one would expect that the increased interfacial contact area between the NP GaN and the $MAPbI_3$ may also increase the probability that interface defects form, which could militate the device performance, a spontaneously forming Ga_2O_3 layer on the surface of the NP GaN (during the

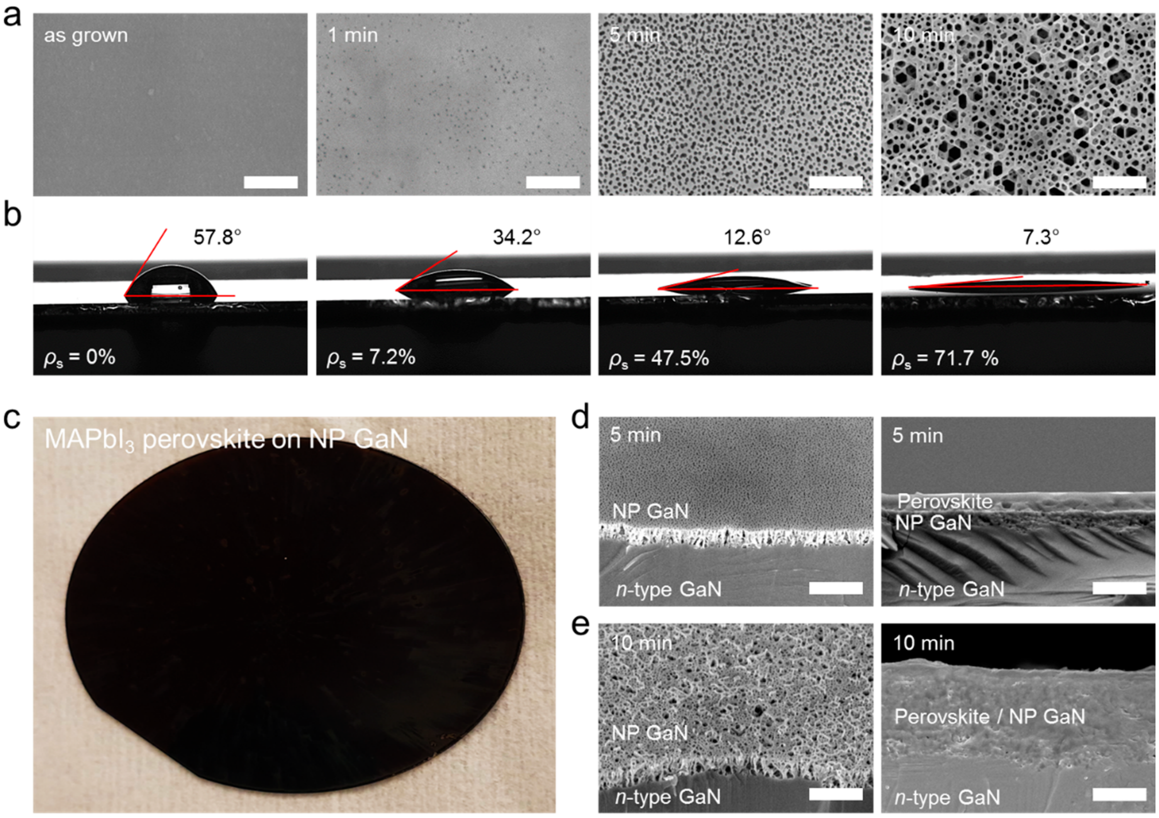

Figure 2. Plan-view scanning electron microscopy (SEM) images of (a) *n*-GaN layer template and NP GaN formed after 1, 5, and 10 min of electrochemical etching. Scale bar is 500 nm. (b) Water contact angle measurement for *n*-GaN template with NP GaN formed after 1, 5, and 10 min of electrochemical etching. (c) Photograph of perovskite MAPbI$_3$ spin-coated thin film on a 2 in. NP GaN wafer. Bird's-eye and cross-sectional SEM images of (d) NP GaN formed after 5 min and (e) 10 min of electrochemical etching. Scale bar is 1.0 μm.

electrochemical etching-fabrication of the NP GaN layer) acts as an interlayer between the perovskite and NP GaN and, thereby, passivating defect-related deep levels. To illustrate these advantages, we demonstrate prototype MAPbI$_3$ PSCs based on this NP GaN/*n*-GaN cathode structure (without any other ETL) with promising power conversion efficiencies (PCEs) of up to 18.79%. Our work shows that III-nitride-based nanostructure can be versatile components in perovskite-based optoelectronics, enabling new device architectures that do away with rate-limiting material layers.

To fabricate NP GaN, the electrochemical etching of *n*-GaN was conducted as shown in Figure 1a. The 10 μm-thick *n*-GaN thin films were grown on the double-polished sapphire substrate to ensure high transmittance to visible light. Figure 1b displays the 2 in. wafers of as-grown *n*-GaN and NP GaN formed by 1, 5, and 10 min of electrochemical etching at an applied bias of 12 V (Figure S1). Upon increasing the etching time, the transmittance of GaN (Figure 1c) was systematically decreased, and the integrated photoluminescence (PL) intensity (Figure 1d) was increased accordingly, because of the scattering effect from the formed nanopores. Figure 1e shows optical and confocal microscopy images of nanopores under a luminous source (450 nm). Photons penetrating the NP GaN interact with the nanopores (D_{avg} = 37.5 nm), leading to Rayleigh scattering. This optical property of NP GaN causes the trajectory of photons to fluctuate, contributing to the enhancement in the light harvesting of the NP GaN medium. In terms of electrical properties, the current flow through NP GaN (denoted as A−A′) was influenced by etching; the resistance was increased by increasing the etching time for the NP GaN structure (Figure 1f) because of the pore volume fraction, including pore interconnection and tortuosity.[51] On the other hand, lateral electrical transport through the *n*-GaN/*n*-GaN structure (denoted as B−B′) showed nearly the same resistivity regardless of the etching time (Figure 1g). Despite the presence of a porous layer along the direction of current flow, the NP GaN structure exhibited a lateral electric conductivity higher than that of a conventional ITO film (Figure 1h). Thus, the NP GaN/*n*-GaN structure serves as a dual-function layer exhibiting properties of both a TCL and an ETL.

To explore the possibility of depositing a perovskite film on NP GaN by spin-coating of a perovskite solution, we conducted contact angle measurements. We calculated the surface area fraction (ρ_s) of NP GaN using plan-view scanning electron microscopy (SEM) images (Figure 2a). Figure 2b shows the contact angles measured for deionized water as a function of ρ_s. The hydrophobicity of the dense *n*-GaN film was indicated by a large contact angle of 57.8°. Increasing the value of ρ_s of NP GaN caused the contact angle to decrease (Figure S2), with angles of 34.2°, 12.6°, and 7.3° measured at ρ_s values of 7.2%, 47.5%, and 71.7%, respectively; this trend clearly reflects the hydrophilicity induced by introducing nanopores into the GaN surface. This result is attributed to the surface roughness and oxidation of the GaN surface to Ga$_2$O$_3$ (or GaO$_3^{3-}$) obtained by electrochemical etching, which induces surface tension energy higher than that observed for an intrinsic dense *n*-GaN surface.[52] After ozone plasma treatment for 10 min, we spin-coated MAPbI$_3$ perovskite onto a 2 in. NP GaN wafer (Figure 2c). Figure 2d,e shows how the

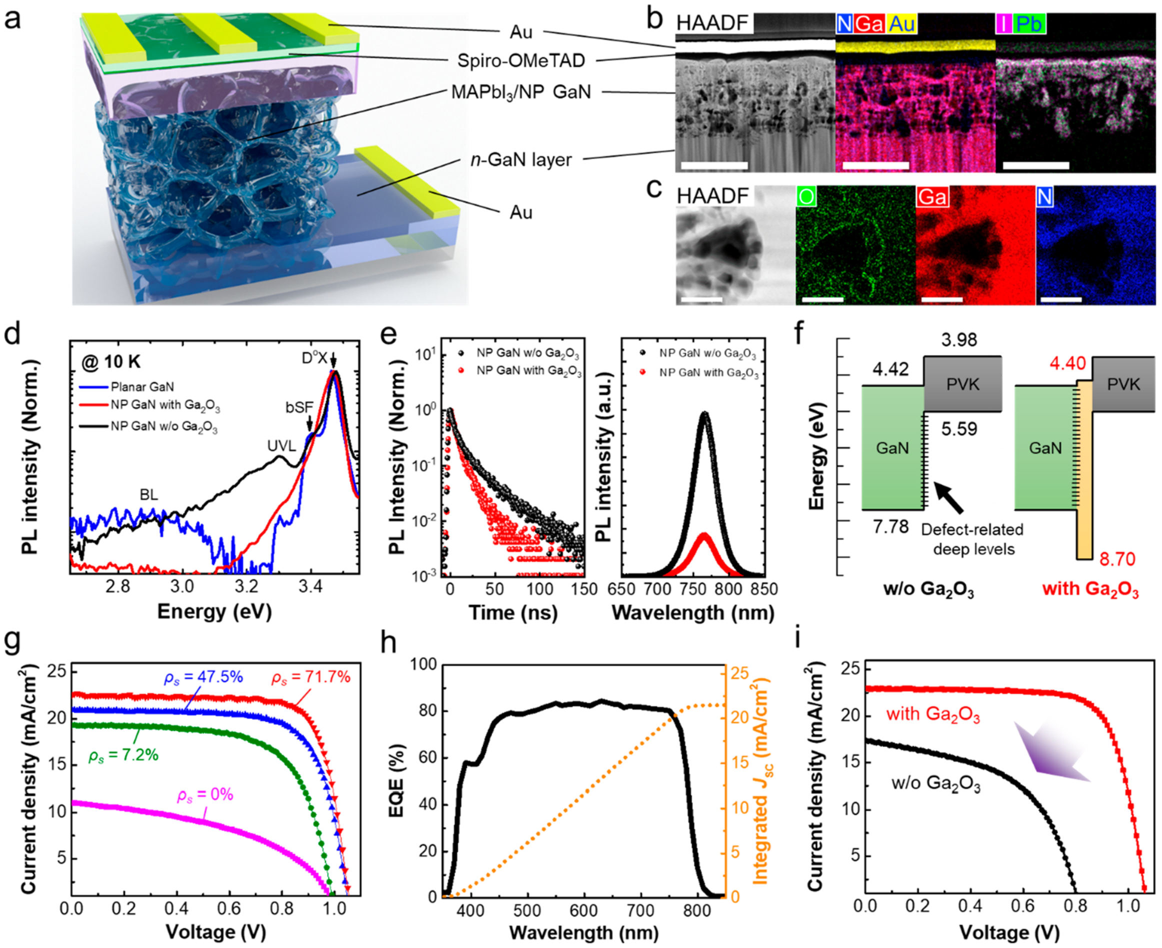

Figure 3. (a) Schematic illustration of the PSC structure including NP GaN/MAPbI$_3$. (b) Cross-sectional high-angle annular dark-field scanning transmission electron microscopy (HAADF-STEM) image of PSC. Energy-dispersive X-ray spectroscopy (EDX) elemental mapping of N, Ga, and Au for the structural overview and of Pb and I confirm that those materials are well incorporated into NP GaN. Scale bar is 1 μm. (c) Cross-sectional HAADF-STEM image of the NP GaN/planar GaN interface and EDX elemental mapping of O, Ga, and N, respectively. Scale bar is 100 nm. (d) Low-temperature (10 K) PL measurements of planar GaN template and NP GaN (with and without Ga$_2$O$_3$) samples for defect study. Comparison of NP GaN with and without Ga$_2$O$_3$ by (e) normalized transient PL decay profile (left) and steady-state PL (right). (f) Comparison of energy band diagrams for devices with and without Ga$_2$O$_3$. (g) Current−voltage characteristics of MAPbI$_3$ PSCs with planar GaN layer and NP GaN structures with porosities of ρ_s = 0, 7.2, 47.5, and 71.7%. (h) Incident photon-to-current efficiency of solar cell using NP GaN (ρ_s = 71.7%) and (i) comparison of current−voltage characteristics for NP GaN/MAPbI$_3$ solar cells with and without Ga$_2$O$_3$ interlayer.

morphology of the MAPbI$_3$ perovskite films varied with the ρ_s of NP GaN as a result of changes in the spin-coating conditions. At high porosities (ρ_s > 71.7%), the perovskite film was embedded in the NP GaN; however, at low porosities (ρ_s < 47.5%), the perovskite film was separated from the NP GaN. These results show that the perovskite could be confined in the nanopores when the ρ_s of the NP GaN layer was sufficiently high (ρ_s > 71.7%). To summarize, NP GaN exhibits the prerequisite optical, electrical, and structural characteristics to be a promising substitute for the current layers employed as ETLs/TCLs in PSC devices.

To confirm that the NP GaN structure can serve as an alternative to conventional ETLs and TCLs, we fabricated proof-of-concept MAPbI$_3$ PSCs based on this structure. Figure 3a shows a schematic illustration of a PSC featuring a NP GaN/MAPbI$_3$ heterostructure. Using planar *n*-GaN, NP GaN was formed by electrochemical etching for different durations. To identify the various layers of the solar cell structure, we cross-sectioned the structure by focused-ion-beam (FIB) processing and then probed the cross-section using transmission electron microscopy (TEM). Figure 3b shows corresponding cross-sectional high-angle annular dark-field scanning transmission microscopy (HAADF-STEM) images. The various layers of the solar cell are visually distinct, and both the planar GaN layer and perovskite-coated NP GaN are clearly shown. In STEM mode, energy-dispersive X-ray spectroscopy (EDX) with element mapping of N, Ga, and Au confirmed that the NP GaN structure remained well intact after solar cell fabrication. Elemental mapping of I and Pb revealed that the perovskite material was well-incorporated deep into the NP GaN structure (Figure S3). Additional EDX mapping for other elements was also performed at the interface of the pristine NP GaN layer without perovskite (Figure 3c). Note that in the area around the interface between the NP GaN and planar GaN layers, the constituent elements (O, Ga, and N) are distributed uniformly throughout the topmost GaN surface of the NP GaN structure. Interestingly, a highly intense peak corresponding to O was found at the edge of the porous structures, suggesting that the Ga$_2$O$_3$ interlayer was formed as an outer shell around the NP GaN. This Ga$_2$O$_3$ likely resulted from the oxalic acid used during the electrochemical etching of NP GaN.

To better understand the role of Ga_2O_3 in NP GaN, we performed a series of optical characterizations on NP GaN samples (with and without Ga_2O_3). To fabricate NP GaN without Ga_2O_3, the sample was cleaned with acetone and isopropanol (IPA) and then rinsed with deionized water in advance. Additional oxides were removed by dipping the sample in buffered oxide etch (BOE) for 5 min. Using a planar GaN layer as a reference, NP GaN samples were examined by low-temperature (10 K) PL measurements to confirm the crystallinity of GaN and analyze several defect states of the NP structures. Figure 3d shows neutral donor bound exciton ($D°X$) peaks around 3.478 eV detected in three samples, which represent the dominant emission spectrum of GaN. These peaks agree well with the $D°X$ peaks reported previously for MOCVD planar GaN layer templates grown on a sapphire substrate.[52] It should be noted that $D°X$ peaks can be observed only in highly crystalline homoepitaxial GaN samples; thus, the electrochemical etching process used to form NP GaN does not degrade the crystal quality of GaN.[53,54] It should also be noted that the PL spectrum of the planar GaN layer sample and that of the NP GaN sample without Ga_2O_3 displayed several interesting features. For instance, a secondary peak around the dominant peak ($D°X \approx 3.4$ eV), attributed to a basal-plane stacking fault (bSF), was observed in the two samples.[55] The bSF emission peak is a well-known intrinsic defect peak and is commonly observed in epitaxially grown GaN. Other defect-related transition lines of ultraviolet luminescence (UVL) near 3.3 eV and blue luminescence (BL) around 2.9−3.0 eV were also observed.[56−58] However, these defect-related bSF, UVL, and BL peaks were observed only in the planar GaN layer sample and NP GaN sample without Ga_2O_3. We speculate that defect-related peaks are effectively suppressed by passivation with a thin Ga_2O_3 layer surrounding NP GaN.

To clarify the passivation effect of the Ga_2O_3 interlayer between the perovskite and NP GaN layers of the heterostructure, we spin-coated $MAPbI_3$ perovskite materials onto two NP GaN samples (with and without Ga_2O_3), and time-resolved PL (TR-PL) with steady-state PL measurements were carried out on both samples at room temperature (Figure 3e). The TR-PL spectrum of $MAPbI_3$ on NP GaN with Ga_2O_3 showed a relatively short PL average lifetime ($t = 10.07$ ns), while $MAPbI_3$ on NP GaN without Ga_2O_3 exhibited a longer PL lifetime ($t = 18.20$ ns, see Table S2). We attribute such short lifetime to the presence of Ga_2O_3 between the $MAPbI_3$ and NP GaN layers, which facilitates the carrier extraction to the *n*-GaN. In the same vein, steady-state PL measurements indicated more pronounced PL quenching of $MAPbI_3$ on NP GaN with Ga_2O_3 than on that without Ga_2O_3. Thus, introducing the Ga_2O_3 interlayer is a useful strategy to suppress nonradiative recombination that occurs as a consequence of defect-related deep levels and energy-band mismatching, as shown in Figure 3f.

To further evaluate the effects of different porosities on NP GaN/$MAPbI_3$ PSCs, we compared the corresponding current−voltage characteristics of the samples using two solar cell characterization methods: *J*−*V* and external quantum efficiency (EQE) measurements. Figure 3g shows the current−voltage characteristics of our best-performing $MAPbI_3$ PSCs with planar *n*-GaN layer and NP GaN structures. The reverse-scan short-circuit current density (J_{SC}), open-circuit voltage (V_{OC}), and fill factor (FF) of the solar cell containing planar *n*-GaN were 11.16 mA/cm^2, 0.99 V, and 46.1%, respectively. The rigid PSCs containing a planar *n*-GaN layer exhibited a best PCE of 5.09%. In contrast, the $MAPbI_3$ PSCs containing NP GaN showed a considerable enhancement in J_{SC}, V_{OC}, and FF (see Table 1). The PCE of the solar cells increased continuously as ρ_s was increased from 7.2% to 47.5% and to 71.7%. When the ρ_s was increased to 71.7%, the rigid PSCs exhibited the best PCE of 18.79%. The corresponding EQE and integrated J_{SC} of a representative solar cell containing NP GaN ($\rho_s = 71.7\%$) is shown in Figure 3h. Figure S4 shows the detailed performance characteristics of our PSCs with NP GaN ($\rho_s = 71.7\%$). To further understand the influence of the Ga_2O_3 interlayer, we also fabricated solar cells from which the Ga_2O_3 interlayer of the NP GaN structure was removed by chemical etching with BOE at room temperature for 5 min (Figure 3i). We observed that the presence of the Ga_2O_3 interlayer between the NP GaN and perovskite layers, which formed spontaneously at the NP GaN surface during the electrochemical etching process, contributes to the increased solar cell efficiency. Our PSC with NP GaN/*n*-GaN exhibits the highest efficiency among published ITO-free PSCs with alternative TCLs (see Table S3).

Table 1. Summary of the J_{sc}, V_{oc}, FF, and PCE Parameters for PSCs with Planar GaN and NP GaN

	J_{SC}	V_{OC}	FF	PCE
Planar GaN ($\rho_s = 0\%$)	11.16 mA/cm^2	0.99 V	46.1%	5.09%
NP GaN ($\rho_s = 7.2\%$)	19.17 mA/cm^2	0.99 V	67.2%	12.75%
NP GaN ($\rho_s = 47.5\%$)	21.08 mA/cm^2	1.05 V	72.8%	16.12%
NP GaN ($\rho_s = 71.7\%$)	22.87 mA/cm^2	1.07 V	76.8%	18.79%

To investigate the light absorption efficiency of the NP GaN/$MAPbI_3$, we performed FDTD simulations. Figure 4a illustrates the simulated structure of the PSC with NP GaN/$MAPbI_3$ under UV and visible light illumination ($\lambda = 350$−800 nm). The dispersion and extinction coefficients of each material (GaN and $MAPbI_3$) were taken from the reported values in the literature.[59,60] To model the effects of the nanopore distribution in the NP GaN, we designed the NP GaN in the FDTD simulations as repeating planes of porosity, ρ_s, such that the porosity per unit volume, ρ_v, is equivalent to its experimentally estimated value. Figure 4b shows the contrast difference in effective refractive index (n_{eff}) of NP GaN/$MAPbI_3$ ($\rho_s = 71.7\%$). The simulated n_{eff} of NP GaN/$MAPbI_3$ shows an intermediate value between GaN's and $MAPbI_3$'s intrinsic refractive indices at all incident lights ($\lambda = 350$ nm − 800 nm), because the two homogeneously mixed materials follow the n_{eff} based on the 2D Maxwell−Garnett theory[61,62] (see the Supporting Information for details). According to the FDTD simulations, Fresnel reflections are significantly suppressed in a PSC structure sequentially consisting of 2.0 μm thick *n*-GaN, NP GaN/$MAPbI_3$, and $MAPbI_3$ with a gradual refractive index change, compared to those of a PSC structure having an abrupt interface and, thus, decreasing photon losses.

Because UV light photocatalytically degrades the $MAPbI_3$[63,64]—and blocking it increases the lifespan of PSCs—we investigated the propagation of UV light ($\lambda = 350$ nm) in the simulated PSC structure. Figure 4c shows that a 2.0 μm thick *n*-GaN layer blocks incident UV light entirely

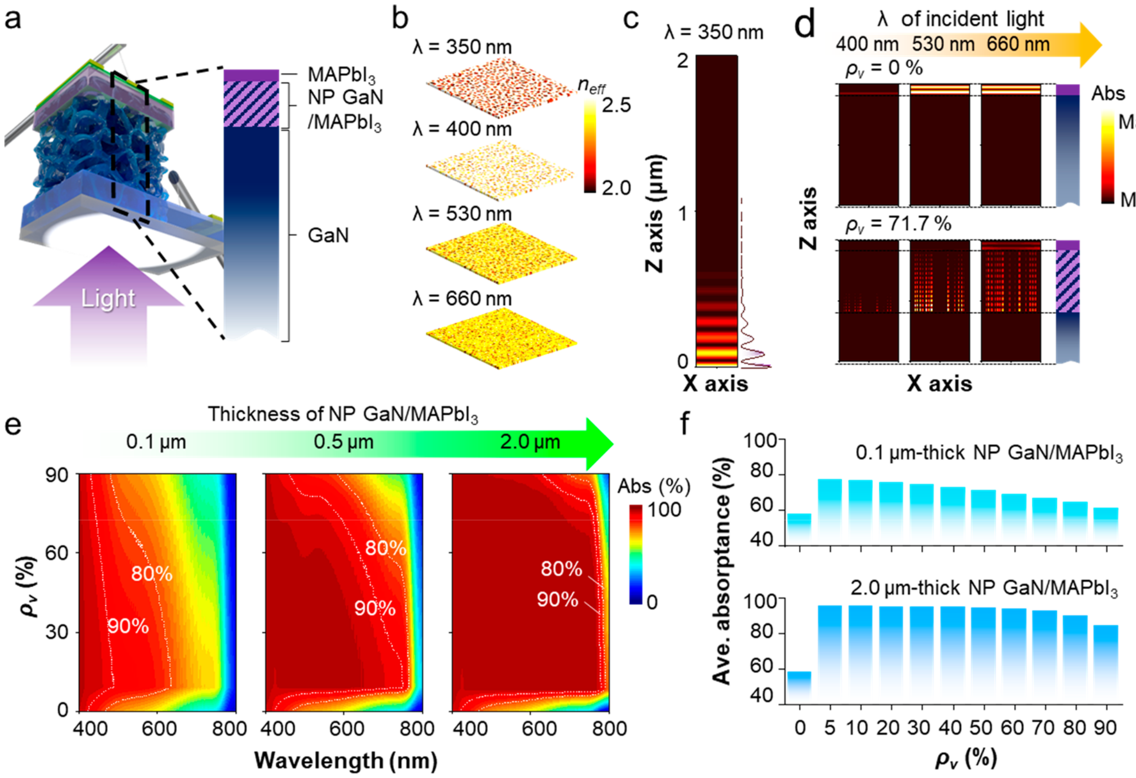

Figure 4. (a) Schematic diagram of the PSC modeled for the FDTD simulation. (b) Contrast difference in effective refractive index (n_{eff}) of NP GaN/MAPbI$_3$ (ρ_s = 71.7%) according to the wavelength of incident light (λ = 350, 400, 530, and 660 nm). Simulated contour maps of the light absorption for (c) planar *n*-GaN layer with UV incident light (λ = 350 nm) and (d) NP GaN/MAPbI$_3$ on *n*-GaN with white light (λ = 400, 530, and 660 nm). ρ_s = 0% (top) consists of MAPbI$_3$ on *n*-GaN without NP GaN, and ρ_s = 71.7% (bottom) consists of NP GaN/MAPbI$_3$ on *n*-GaN with a volume ratio of NP GaN (28.3%) and MAPbI$_3$ (71.7%) filling nanopores of the NP GaN. (e) Simulated contour maps for the absorption spectra of NP GaN/MAPbI$_3$ in the visible light region as functions of the porosity and thickness of NP GaN/MAPbI$_3$ light absorber. Two dashed lines in contour maps indicate the criteria for 80% and 90% of the incident light absorptance. (f) The averaged light absorptance of 0.1 (top) and 2.0 μm-thick (bottom) NP GaN/MAPbI$_3$ with varying ρ_v, respectively.

from reaching the NP GaN/MAPbI$_3$ or MAPbI$_3$ perovskite light absorber layers.

In contrast, light within the visible spectrum (λ = 400, 530, and 660 nm) penetrated the PSC structures and was only absorbed by the perovskite within the MAPbI$_3$ and NP GaN/MAPbI$_3$ layers (see Figure 4d for the simulated absorption profiles). Interestingly, the PSC with NP GaN/MAPbI$_3$ shows an extended absorption distribution along the entire NP GaN/MAPbI$_3$, implying that the hierarchical configuration of NP GaN/MAPbI$_3$ further increases the probability of light absorption.

To analyze the porosity- and thickness-dependent light absorption efficiencies, we performed RCWA simulations. Figure 4e shows the contour maps of calculated light absorptance (λ = 400−800 nm) by increasing the thickness of NP GaN/MAPbI$_3$ and the porosity of NP GaN. The two dashed white lines demarcate the region of the graph for 80% and 90% of the incident light absorptance according to the porosity of NP GaN. This result reveals that when the porosity of NP GaN is between 10% and 80%, the structure shows high absorption for visible light. Moreover, when the NP GaN/MAPbI$_3$ light absorber has a thickness of more than 2.0 μm, perfect absorption occurs throughout the visible light regions. Figure 4f shows the average light absorptance of 0.1 and 2.0 μm-thick NP GaN/MAPbI$_3$ across the entire visible wavelengths. The simulation results suggest that the optimal porosity of NP GaN and the optimal thickness of the NP GaN/MAPbI$_3$ should be between 10% and 80% and ≥2.0 μm, respectively.

In conclusion, the cathode structure in a PSC plays a key role in the extraction of photogenerated electrons. Therefore, one of the most critical aspects of PSC fabrication is finding a suitable combination of a TCL and an ETL, which are typically composed of differing materials, to form the cathode structure. In this respect, we proposed a novel cathode structure for PSCs: a NP GaN/*n*-GaN that combines the function of both the TCL and ETL. The NP GaN/*n*-GaN structure affords enhanced light harvesting (as a result of the structure's gradual refractive index change) and efficient carrier extraction due to the enlarged perovskite interface with the cathode. A Ga$_2$O$_3$ interlayer (formed spontaneously at the surface of the NP GaN layer during the electrochemical etching process) between NP GaN and perovskite contributes to interface passivation. These advantageous properties enabled the fabrication of MAPbI$_3$ PSCs based on NP GaN/*n*-GaN structures that show promising PCEs of up to 18.79%. Our work opens an avenue for PSCs to benefit from the versatile heterostructures afforded by the mature III-nitride-based technologies.

■ ASSOCIATED CONTENT

Supporting Information

The Supporting Information is available free of charge at https://pubs.acs.org/doi/10.1021/acsenergylett.0c01621.

Experimental details of n-GaN growth, electrochemical etching process, TEM, device fabrication, current–voltage characteristics, EQE measurement, FDTD simulation, PL, and TRPL (PDF)

■ AUTHOR INFORMATION

Corresponding Authors

Boon S. Ooi – *Photonics Laboratory, Computer, Electrical and Mathematical Sciences and Engineering Division, King Abdullah University of Science and Technology (KAUST), Thuwal 23955-6900, Kingdom of Saudi Arabia*; Email: boon.ooi@kaust.edu.sa

Osman M. Bakr – *Division of Physical Sciences and Engineering and KAUST Catalyst Center (KCC), King Abdullah University of Science and Technology (KAUST), Thuwal 23955-6900, Kingdom of Saudi Arabia*; orcid.org/0000-0002-3428-1002; Email: osman.bakr@kaust.edu.sa

Authors

Kwang Jae Lee – *Division of Physical Sciences and Engineering and KAUST Catalyst Center (KCC), King Abdullah University of Science and Technology (KAUST), Thuwal 23955-6900, Kingdom of Saudi Arabia*; orcid.org/0000-0002-3158-7532

Jung-Wook Min – *Photonics Laboratory, Computer, Electrical and Mathematical Sciences and Engineering Division, King Abdullah University of Science and Technology (KAUST), Thuwal 23955-6900, Kingdom of Saudi Arabia*; orcid.org/0000-0002-7570-1739

Bekir Turedi – *Division of Physical Sciences and Engineering and KAUST Catalyst Center (KCC), King Abdullah University of Science and Technology (KAUST), Thuwal 23955-6900, Kingdom of Saudi Arabia*

Abdullah Y. Alsalloum – *Division of Physical Sciences and Engineering and KAUST Catalyst Center (KCC), King Abdullah University of Science and Technology (KAUST), Thuwal 23955-6900, Kingdom of Saudi Arabia*; orcid.org/0000-0001-8988-1307

Jung-Hong Min – *Photonics Laboratory, Computer, Electrical and Mathematical Sciences and Engineering Division, King Abdullah University of Science and Technology (KAUST), Thuwal 23955-6900, Kingdom of Saudi Arabia*

Yeong Jae Kim – *School of Electrical Engineering and Computer Science, Gwangju Institute of Science and Technology, Gwangju 61005, Republic of Korea*; orcid.org/0000-0002-0870-9044

Young Jin Yoo – *School of Electrical Engineering and Computer Science, Gwangju Institute of Science and Technology, Gwangju 61005, Republic of Korea*

Semi Oh – *School of Materials Science and Engineering, Gwangju Institute of Science and Technology, Gwangju 61005, Republic of Korea*

Namchul Cho – *Department of Energy Systems Engineering, Soonchunhyang University, Asan 31538, Republic of Korea*

Ram Chandra Subedi – *Photonics Laboratory, Computer, Electrical and Mathematical Sciences and Engineering Division, King Abdullah University of Science and Technology (KAUST), Thuwal 23955-6900, Kingdom of Saudi Arabia*; orcid.org/0000-0003-2818-1352

Somak Mitra – *Semiconductor and Material Spectroscopy Laboratory, Material Science & Engineering Division, King Abdullah University of Science and Technology (KAUST), Thuwal 23955-6900, Kingdom of Saudi Arabia*

Sang Eun Yoon – *Department of Molecular Science and Technology, Ajou University, Suwon 16499, Republic of Korea*

Jong H. Kim – *Department of Molecular Science and Technology, Ajou University, Suwon 16499, Republic of Korea*; orcid.org/0000-0001-6782-2154

Kwangwook Park – *Division of Advanced Materials Engineering, Jeonbuk National University, Jeonju 54896, Republic of Korea*; orcid.org/0000-0002-4600-4600

Tae-Hoon Chung – *Light Source Research Division, Korea Photonics Technology Institute (KOPTI), Gwangju 61007, Republic of Korea*

Sung Hoon Jung – *Light Source Research Division, Korea Photonics Technology Institute (KOPTI), Gwangju 61007, Republic of Korea*

Jong H. Baek – *Light Source Research Division, Korea Photonics Technology Institute (KOPTI), Gwangju 61007, Republic of Korea*

Young Min Song – *School of Electrical Engineering and Computer Science, Gwangju Institute of Science and Technology, Gwangju 61005, Republic of Korea*; orcid.org/0000-0002-4473-6883

Iman S. Roqan – *Semiconductor and Material Spectroscopy Laboratory, Material Science & Engineering Division, King Abdullah University of Science and Technology (KAUST), Thuwal 23955-6900, Kingdom of Saudi Arabia*; orcid.org/0000-0001-7442-4330

Tien Khee Ng – *Photonics Laboratory, Computer, Electrical and Mathematical Sciences and Engineering Division, King Abdullah University of Science and Technology (KAUST), Thuwal 23955-6900, Kingdom of Saudi Arabia*; orcid.org/0000-0002-1480-6975

Complete contact information is available at:
https://pubs.acs.org/10.1021/acsenergylett.0c01621

Author Contributions

+K.J.L and J.-W.M. contributed equally to this work.

Notes

The authors declare no competing financial interest.

■ ACKNOWLEDGMENTS

The authors gratefully acknowledge the financial support provided by King Abdullah University of Science and Technology (KAUST); and the Basic Science Research Program through the National Research Foundation of Korea(NRF) funded by the Ministry of Science, ICT & Future Planning under Grant No. NRF-2019R1A4A1021237.

■ REFERENCES

(1) Zheng, X.; Hou, Y.; Bao, C.; Yin, J.; Yuan, F.; Huang, Z.; Song, K.; Liu, J.; Troughton, J.; Gasparini, N.; et al. Managing Grains and Interfaces via Ligand Anchoring Enables 22.3%-Efficiency Inverted Perovskite Solar Cells. *Nat. Energy* **2020**, *5* (2), 131–140.

(2) Zheng, X.; Troughton, J.; Gasparini, N.; Lin, Y.; Wei, M.; Hou, Y.; Liu, J.; Song, K.; Chen, Z.; Yang, C.; et al. Quantum Dots Supply Bulk-and Surface-Passivation Agents for Efficient and Stable Perovskite Solar Cells. *Joule* **2019**, *3* (8), 1963–1976.

(3) Green, M. A.; Ho-Baillie, A.; Snaith, H. J. The Emergence of Perovskite Solar Cells. *Nat. Photonics* **2014**, *8* (7), 506.

(4) Arora, N.; Dar, M. I.; Hinderhofer, A.; Pellet, N.; Schreiber, F.; Zakeeruddin, S. M.; Grätzel, M. Perovskite Solar Cells with CuSCN Hole Extraction Layers Yield Stabilized Efficiencies Greater than 20%. *Science (Washington, DC, U. S.)* **2017**, *358* (6364), 768–771.

(5) Saliba, M.; Matsui, T.; Seo, J.-Y.; Domanski, K.; Correa-Baena, J.-P.; Nazeeruddin, M. K.; Zakeeruddin, S. M.; Tress, W.; Abate, A.; Hagfeldt, A.; et al. Cesium-Containing Triple Cation Perovskite Solar Cells: Improved Stability, Reproducibility and High Efficiency. *Energy Environ. Sci.* **2016**, *9* (6), 1989−1997.

(6) Wang, Y.; Dar, M. I.; Ono, L. K.; Zhang, T.; Kan, M.; Li, Y.; Zhang, L.; Wang, X.; Yang, Y.; Gao, X.; et al. Thermodynamically Stabilized β-CsPbI3−Based Perovskite Solar Cells with Efficiencies> 18%. *Science (Washington, DC, U. S.)* **2019**, *365* (6453), 591−595.

(7) Chen, R.; Cao, J.; Duan, Y.; Hui, Y.; Chuong, T. T.; Ou, D.; Han, F.; Cheng, F.; Huang, X.; Wu, B.; et al. High-Efficiency, Hysteresis-Less, UV-Stable Perovskite Solar Cells with Cascade ZnO−ZnS Electron Transport Layer. *J. Am. Chem. Soc.* **2019**, *141* (1), 541−547.

(8) Nie, W.; Tsai, H.; Asadpour, R.; Blancon, J.-C.; Neukirch, A. J.; Gupta, G.; Crochet, J. J.; Chhowalla, M.; Tretiak, S.; Alam, M. A.; et al. High-Efficiency Solution-Processed Perovskite Solar Cells with Millimeter-Scale Grains. *Science (Washington, DC, U. S.)* **2015**, *347* (6221), 522−525.

(9) Chen, Z.; Turedi, B.; Alsalloum, A. Y.; Yang, C.; Zheng, X.; Gereige, I.; AlSaggaf, A.; Mohammed, O. F.; Bakr, O. M. Single-Crystal MAPbI3 Perovskite Solar Cells Exceeding 21% Power Conversion Efficiency. *ACS Energy Lett.* **2019**, *4* (6), 1258−1259.

(10) Alsalloum, A. Y.; Turedi, B.; Zheng, X.; Mitra, S.; Zhumekenov, A. A.; Lee, K. J.; Maity, P.; Gereige, I.; AlSaggaf, A.; Roqan, I. S.; et al. Low-Temperature Crystallization Enables 21.9% Efficient Single-Crystal MAPbI3 Inverted Perovskite Solar Cells. *ACS Energy Lett.* **2020**, *5* (2), 657−662.

(11) Liu, M.; Johnston, M. B.; Snaith, H. J. Efficient Planar Heterojunction Perovskite Solar Cells by Vapour Deposition. *Nature* **2013**, *501* (7467), 395−398.

(12) Lee, K. J.; Turedi, B.; Sinatra, L.; Zhumekenov, A. A.; Maity, P.; Dursun, I.; Naphade, R.; Merdad, N.; Alsalloum, A.; Oh, S.; et al. Perovskite-Based Artificial Multiple Quantum Wells. *Nano Lett.* **2019**, *19* (6), 3535−3542.

(13) Turren-Cruz, S.-H.; Hagfeldt, A.; Saliba, M. Methylammonium-Free, High-Performance, and Stable Perovskite Solar Cells on a Planar Architecture. *Science (Washington, DC, U. S.)* **2018**, *362* (6413), 449−453.

(14) Qiu, L.; He, S.; Ono, L. K.; Liu, S.; Qi, Y. Scalable Fabrication of Metal Halide Perovskite Solar Cells and Modules. *ACS Energy Lett.* **2019**, *4* (9), 2147−2167.

(15) Carlson, D. E.; Wronski, C. R. Amorphous Silicon Solar Cell. *Appl. Phys. Lett.* **1976**, *28* (11), 671−673.

(16) Hamaker, H. C.; Ford, C. W.; Werthen, J. G.; Virshup, G. F.; Kaminar, N. R.; King, D. L.; Gee, J. M. 26% Efficient Magnesium-doped AlGaAs/GaAs Solar Concentrator Cells. *Appl. Phys. Lett.* **1985**, *47* (7), 762−764.

(17) Shin, I.-S.; Kim, J.; Lee, D.; Kim, D.; Park, Y.; Yoon, E. Epitaxial Growth of Single-Crystalline AlN Layer on Si (111) by DC Magnetron Sputtering at Room Temperature. *Jpn. J. Appl. Phys.* **2018**, *57* (6), 060306.

(18) Singh, R.; Giri, A.; Pal, M.; Thiyagarajan, K.; Kwak, J.; Lee, J.-J.; Jeong, U.; Cho, K. Perovskite Solar Cells with an MoS 2 Electron Transport Layer. *J. Mater. Chem. A* **2019**, *7* (12), 7151−7158.

(19) Wang, Y.; Wan, J.; Ding, J.; Hu, J.; Wang, D. A Rutile TiO2 Electron Transport Layer for the Enhancement of Charge Collection for Efficient Perovskite Solar Cells. *Angew. Chem., Int. Ed.* **2019**, *58* (28), 9414−9418.

(20) Son, D.-Y.; Im, J.-H.; Kim, H.-S.; Park, N.-G. 11% Efficient Perovskite Solar Cell Based on ZnO Nanorods: An Effective Charge Collection System. *J. Phys. Chem. C* **2014**, *118* (30), 16567−16573.

(21) Chen, Y.; Meng, Q.; Zhang, L.; Han, C.; Gao, H.; Zhang, Y.; Yan, H. SnO2-Based Electron Transporting Layer Materials for Perovskite Solar Cells: A Review of Recent Progress. *J. Energy Chem.* **2019**, *35*, 144−167.

(22) Guo, H.; Chen, H.; Zhang, H.; Huang, X.; Yang, J.; Wang, B.; Li, Y.; Wang, L.; Niu, X.; Wang, Z. Low-Temperature Processed Yttrium-Doped SrSnO3 Perovskite Electron Transport Layer for Planar Heterojunction Perovskite Solar Cells with High Efficiency. *Nano Energy* **2019**, *59*, 1−9.

(23) Zhu, Z.; Zhao, D.; Chueh, C.-C.; Shi, X.; Li, Z.; Jen, A. K.-Y. Highly Efficient and Stable Perovskite Solar Cells Enabled by All-Crosslinked Charge-Transporting Layers. *Joule* **2018**, *2* (1), 168−183.

(24) Mahmood, K.; Sarwar, S.; Mehran, M. T. Current Status of Electron Transport Layers in Perovskite Solar Cells: Materials and Properties. *RSC Adv.* **2017**, *7* (28), 17044−17062.

(25) Tavakoli, M. M.; Tavakoli, R.; Yadav, P.; Kong, J. A Graphene/ZnO Electron Transfer Layer Together with Perovskite Passivation Enables Highly Efficient and Stable Perovskite Solar Cells. *J. Mater. Chem. A* **2019**, *7* (2), 679−686.

(26) Xiong, L.; Guo, Y.; Wen, J.; Liu, H.; Yang, G.; Qin, P.; Fang, G. Review on the Application of SnO2 in Perovskite Solar Cells. *Adv. Funct. Mater.* **2018**, *28* (35), 1802757.

(27) Docampo, P.; Ball, J. M.; Darwich, M.; Eperon, G. E.; Snaith, H. J. Efficient Organometal Trihalide Perovskite Planar-Heterojunction Solar Cells on Flexible Polymer Substrates. *Nat. Commun.* **2013**, *4* (1), 2761.

(28) Yu, H.; Lee, J. W.; Yun, J.; Lee, K.; Ryu, J.; Lee, J.; Hwang, D.; Kim, S. K.; Jang, J. Outstanding Performance of Hole-Blocking Layer-Free Perovskite Solar Cell Using Hierarchically Porous Fluorine-Doped Tin Oxide Substrate. *Adv. Energy Mater.* **2017**, *7* (22), 1700749.

(29) Ye, S.; Rathmell, A. R.; Chen, Z.; Stewart, I. E.; Wiley, B. J. Metal Nanowire Networks: The next Generation of Transparent Conductors. *Adv. Mater.* **2014**, *26* (39), 6670−6687.

(30) Service, R. F. Nations Move to Head off Shortages of Rare Earths. *Science* **2010**, *327*, 1596.

(31) Nakamura, E.; Sato, K. Managing the Scarcity of Chemical Elements. *Nat. Mater.* **2011**, *10* (3), 158−161.

(32) Poncé, S.; Jena, D.; Giustino, F. Route to High Hole Mobility in GaN via Reversal of Crystal-Field Splitting. *Phys. Rev. Lett.* **2019**, *123* (9), 96602.

(33) Levinshtein, M. E.; Rumyantsev, S. L.; Shur, M. S. *Properties of Advanced Semiconductor Materials: GaN, AIN, InN, BN, SiC, SiGe*; John Wiley & Sons, 2001.

(34) Lee, K. J.; Kim, S.-J.; Kim, J.-J.; Hwang, K.; Kim, S.-T.; Park, S.-J. Enhanced Performance of InGaN/GaN Multiple-Quantum-Well Light-Emitting Diodes Grown on Nanoporous GaN Layers. *Opt. Express* **2014**, *22* (104), A1164−A1173.

(35) Prabaswara, A.; Min, J.-W.; Zhao, C.; Janjua, B.; Zhang, D.; Albadri, A. M.; Alyamani, A. Y.; Ng, T. K.; Ooi, B. S. Direct Growth of III-Nitride Nanowire-Based Yellow Light-Emitting Diode on Amorphous Quartz Using Thin Ti Interlayer. *Nanoscale Res. Lett.* **2018**, *13* (1), 41.

(36) Schmidt, M. C.; Kim, K.-C.; Farrell, R. M.; Feezell, D. F.; Cohen, D. A.; Saito, M.; Fujito, K.; Speck, J. S.; DenBaars, S. P.; Nakamura, S. Demonstration of Nonpolar M-Plane InGaN/GaN Laser Diodes. *Jpn. J. Appl. Phys.* **2007**, *46* (3L), L190.

(37) Binet, F.; Duboz, J. Y.; Rosencher, E.; Scholz, F.; Härle, V. Mechanisms of Recombination in GaN Photodetectors. *Appl. Phys. Lett.* **1996**, *69* (9), 1202−1204.

(38) Lim, K. T. P.; Deakin, C.; Ding, B.; Bai, X.; Griffin, P.; Zhu, T.; Oliver, R. A.; Credgington, D. Encapsulation of Methylammonium Lead Bromide Perovskite in Nanoporous GaN. *APL Mater.* **2019**, *7* (2), 021107.

(39) Zhou, H.; Mei, J.; Xue, M.; Song, Z.; Wang, H. High-Stability, Self-Powered Perovskite Photodetector Based on a CH3NH3PbI3/GaN Heterojunction with C60 as an Electron Transport Layer. *J. Phys. Chem. C* **2017**, *121* (39), 21541−21545.

(40) Gong, J.; Liu, S.; He, Y.; Feng, X.; Xia, X.; Quan, Z.; Wang, L. Study on the Band Alignment of GaN/CH3NH3PbBr3 Heterojunction by x-Ray Photoelectron Spectroscopy. *Appl. Phys. Lett.* **2017**, *111* (12), 122103.

(41) Wang, Y.; Zheng, D.; Li, L.; Zhang, Y. Enhanced Efficiency of Flexible GaN/Perovskite Solar Cells Based on the Piezo-Phototronic Effect. *ACS Appl. Energy Mater.* **2018**, *1* (7), 3063−3069.

(42) Chen, S.; Zhang, C.; Lee, J.; Han, J.; Nurmikko, A. High-Q, Low-Threshold Monolithic Perovskite Thin-Film Vertical-Cavity Lasers. *Adv. Mater.* **2017**, *29* (16), 1604781.

(43) Nakamura, S.; Harada, Y.; Seno, M. Novel Metalorganic Chemical Vapor Deposition System for GaN Growth. *Appl. Phys. Lett.* **1991**, *58* (18), 2021−2023.

(44) Fujito, K.; Kubo, S.; Nagaoka, H.; Mochizuki, T.; Namita, H.; Nagao, S. Bulk GaN Crystals Grown by HVPE. *J. Cryst. Growth* **2009**, *311* (10), 3011−3014.

(45) Kočan, M.; Rizzi, A.; Lüth, H.; Keller, S.; Mishra, U. K. Surface Potential at As-Grown GaN (0001) MBE Layers. *Phys. Status Solidi B* **2002**, *234* (3), 773−777.

(46) Kim, D. H.; Kumar, V.; Chen, G.; Dabiran, A. M.; Wowchak, A. M.; Osinsky, A.; Adesida, I. ALD Al2O3 Passivated MBE-Grown AlGaN/GaN HEMTs on 6H-SiC. *Electron. Lett.* **2007**, *43* (2), 127−128.

(47) Nonomura, S.; Kobayashi, S.; Gotoh, T.; Hirata, S.; Ohmori, T.; Itoh, T.; Nitta, S.; Morigaki, K. Photoconductive A-GaN Prepared by Reactive Sputtering. *J. Non-Cryst. Solids* **1996**, *198*, 174−177.

(48) Choi, J. H.; Zoulkarneev, A.; Kim, S. Il; Baik, C. W.; Yang, M. H.; Park, S. S.; Suh, H.; Kim, U. J.; Son, H. Bin; Lee, J. S.; et al. Nearly Single-Crystalline GaN Light-Emitting Diodes on Amorphous Glass Substrates. *Nat. Photonics* **2011**, *5* (12), 763−769.

(49) Zou, C. W.; Wang, H. J.; Yin, M. L.; Li, M.; Liu, C. S.; Guo, L. P.; Fu, D. J.; Kang, T. W. Preparation of GaN Films on Glass Substrates by Middle Frequency Magnetron Sputtering. *J. Cryst. Growth* **2009**, *311* (2), 223−227.

(50) Lye, K. S.; Kobayashi, A.; Ueno, K.; Ohta, J.; Fujioka, H. InN Thin-Film Transistors Fabricated on Polymer Sheets Using Pulsed Sputtering Deposition at Room Temperature. *Appl. Phys. Lett.* **2016**, *109* (3), 032106.

(51) Cai, J.; Wei, W.; Hu, X.; Wood, D. A. Electrical Conductivity Models in Saturated Porous Media: A Review. *Earth-Sci. Rev.* **2017**, *171*, 419−433.

(52) Lee, K. J.; Chun, J.; Kim, S.-J.; Oh, S.; Ha, C.-S.; Park, J.-W.; Lee, S.-J.; Song, J.-C.; Baek, J. H.; Park, S.-J. Enhanced Optical Output Power of InGaN/GaN Light-Emitting Diodes Grown on a Silicon (111) Substrate with a Nanoporous GaN Layer. *Opt. Express* **2016**, *24* (5), 4391−4398.

(53) Viswanath, A. K.; Lee, J. I.; Yu, S.; Kim, D.; Choi, Y.; Hong, C. Photoluminescence Studies of Excitonic Transitions in GaN Epitaxial Layers. *J. Appl. Phys.* **1998**, *84* (7), 3848−3859.

(54) Monemar, B. Bound Excitons in GaN. *J. Phys.: Condens. Matter* **2001**, *13* (32), 7011.

(55) Forsberg, M.; Serban, A.; Poenaru, I.; Hsiao, C.-L.; Junaid, M.; Birch, J.; Pozina, G. Stacking Fault Related Luminescence in GaN Nanorods. *Nanotechnology* **2015**, *26* (35), 355203.

(56) Reshchikov, M. A. Determination of Acceptor Concentration in GaN from Photoluminescence. *Appl. Phys. Lett.* **2006**, *88* (20), 202104.

(57) Reshchikov, M. A.; Morkoç, H. Luminescence from Defects in GaN. *Phys. B* **2006**, *376*, 428−431.

(58) Reshchikov, M. A.; Morkoç, H. Luminescence Properties of Defects in GaN. *J. Appl. Phys.* **2005**, *97* (6), 061301.

(59) Kim, Y. J.; Lee, G. J.; Kim, S.; Min, J.-W.; Jeong, S. Y.; Yoo, Y. J.; Lee, S.; Song, Y. M. Efficient Light Absorption by GaN Truncated Nanocones for High Performance Water Splitting Applications. *ACS Appl. Mater. Interfaces* **2018**, *10* (34), 28672−28678.

(60) Leguy, A. M. A.; Azarhoosh, P.; Alonso, M. I.; Campoy-Quiles, M.; Weber, O. J.; Yao, J.; Bryant, D.; Weller, M. T.; Nelson, J.; Walsh, A.; et al. Experimental and Theoretical Optical Properties of Methylammonium Lead Halide Perovskites. *Nanoscale* **2016**, *8* (12), 6317−6327.

(61) Hutchinson, N. J.; Coquil, T.; Richman, E. K.; Tolbert, S. H.; Pilon, L. Reflectance of Surfactant-Templated Mesoporous Silica Thin Films: Simulations versus Experiments. *Thin Solid Films* **2010**, *518* (8), 2134−2140.

(62) Hulkkonen, H. H.; Salminen, T.; Niemi, T. Block Copolymer Patterning for Creating Porous Silicon Thin Films with Tunable Refractive Indices. *ACS Appl. Mater. Interfaces* **2017**, *9* (37), 31260−31265.

(63) Li, Y.; Xu, X.; Wang, C.; Ecker, B.; Yang, J.; Huang, J.; Gao, Y. Light-Induced Degradation of CH3NH3PbI3 Hybrid Perovskite Thin Film. *J. Phys. Chem. C* **2017**, *121* (7), 3904−3910.

(64) Abdelmageed, G.; Jewell, L.; Hellier, K.; Seymour, L.; Luo, B.; Bridges, F.; Zhang, J. Z.; Carter, S. Mechanisms for Light Induced Degradation in MAPbI3 Perovskite Thin Films and Solar Cells. *Appl. Phys. Lett.* **2016**, *109* (23), 233905.